Hydrogen Adsorption on Ordered and Disordered Pt-Ni Alloys

Shengjie Zhang,[1] Duane D. Johnson,[2,3] William A. Shelton,[1,3,4] and Ye Xu[1]*

[1] *Cain Department of Chemical Engineering, Louisiana State University, Baton Rouge, LA 70803, USA*

[2] *Department of Materials Science & Engineering, Iowa State University, Ames, IA 50011, USA*

[3] *Ames Laboratory, U.S. Department of Energy, Ames, IA 50011, USA*

[4] *Center for Computation and Technology, Louisiana State University, Baton Rouge, LA 70803, USA*

Abstract

The bulk properties and chemical reactivity of disordered Pt-Ni alloys in the A1 (*fcc*) structure are investigated using different methods: Virtual Crystal Approximation (VCA), Korringa–Kohn–Rostoker Coherent Potential Approximation (KKR-CPA), and large explicit supercells generated using Super-Cell Random Approximates (SCRAPs). While VCA predicts lattice constants that closely follow Vegard's law, the large supercells and KKR-CPA predict lattice constants that are consistently larger than Vegard's law. KKR-CPA results closely agree with those from the large supercells for the disordered alloys, producing similar projected density of states and magnetic moment across the composition range. For instance, while VCA predicts the disordered alloys to be non-magnetic at a Pt concentration (x_{Pt}) $\geq$ 0.5, KKR-CPA and SCRAPs predict the disordered alloys to remain ferromagnetic to higher Pt concentrations. As x_{Pt} decreases, the adsorption of H becomes more exothermic on bulk-terminated (111) surfaces but less exothermic on Pt monolayer-terminated (111) surfaces due largely to strain effects. (111) surfaces cut from the large supercells predict average H adsorption energies on the disordered alloys similar to those on the ordered phases of the same compositions, while VCA predicts H adsorption to be more exothermic.

Introduction

Over the past few decades, Pt-based alloys have been actively researched as electrocatalysts for hydrogen evolution reaction (HER) and oxygen reduction reaction (ORR), both for improved catalytic properties and for reduced precious metal usage compared to monometallic Pt catalysts. Significant examples include Pt-3d metal alloys (e.g., Fe, Co, and Ni, at a Pt atomic concentration $x_{Pt} \geq 0.5$) [1-5], Pt-lanthanide and Pt-alkaline earth alloys (e.g. Tb, Gd, Ca, and La, at a composition of Pt_5M) [6], BiPt surface alloy [7], and Pt overlayer or Pt shell structures [8-11]. Enhancements for HER and ORR activity ranging from a few times to dozens of times that of Pt have been reported.

A factor that potentially affects the catalytic activity of Pt alloys but is less well recognized, is the phase in which an alloy is formed. Fe and Co, for instance, form ordered face centered tetragonal (*fct*) $L1_0$ phases with a composition of PtM (1:1 atomic ratio) and ordered face centered cubic (*fcc*) $L1_2$ phases with a composition of Pt_3M (3:1 atomic ratio). In addition to the ordered $L1_0$ and $L1_2$ phases, these 3d metals can also form *fcc* solid solutions with Pt (designated as A1, α, or γ phase in different literature) for all compositions, including in off-stoichiometry or at $x_{Pt} < 0.5$. For Ni, the existence of an ordered $L1_2$ phase for Pt_3Ni is not clear [12] and only a random solid solution may be possible [4,13]. An ordered *fcc* $L1_2$ phase for PtM_3 may exist, but the experimental evidence is inconclusive. Computationally determined phase diagrams do predict $L1_2$ PtM_3 and Pt_3M phases for Pt-Fe, Pt-Co, and Pt-Ni [14]. In traditional alloy research, "disordered alloys" usually refer to random mixtures of metals that have overall well-defined crystal structures yet whose component elements do not form any well-defined ordered sub-lattices. We employ this standard terminology in this work.

Differences due to order vs. disorder in Pt-M alloys have been explored in a handful of

electrochemical studies. In some studies, the purported disordered samples (Pt-Fe [15-17], Pt-Co [18], Pt-Ni [19]) were obtained by annealing precursors at temperatures well below the established order/disorder transition temperatures (e.g. 1300, 825, and 645 ºC for PtFe, PtCo, PtNi; 750 ºC for Pt_3Co) [12], which likely resulted in materials that had heterogeneous local structures or compositions, or were phase-separated. Some workers annealed precursors (e.g. Pt-Co [20,21]; Pt-Fe, Pt-Ni, and Pt-Cu [22]; Pt-Co, Pt-Ni, and Pt-Cr [23]) above the order/disorder transition temperature and allowed them to cool down slowly. This approach likely produced ordered phases (i.e. Pt_3Co, PtCo) that most closely corresponded to the compositions of the starting materials, with possible Pt segregation. Rapid quenching following annealing is necessary to produce true A1 Pt-M phases [24,25]. Due to a lack of consistency in the literature, the lattice constants of A1 Pt-M phases remain unclear. For instance, Watanabe et al. [24] reported the A1 $Pt_{0.75}Co_{0.25}$ phase to have a lattice constant of 3.803 Å, which is smaller than that of the ordered $L1_2$ Pt_3Co phase (3.854 Å; values ranging 3.84~3.87 Å having also been reported [18,23]). Yet later Toda et al. [2] reported 3.86 Å for a disordered $Pt_{0.71}Co_{0.29}$ sample made by simultaneously sputtering Co and Pt at room temperature. This highlights the importance of synthetic routes and processing on the observed properties of alloys.

A related issue is the formation of Pt overlayers, or “skin”. A slow cooling procedure favors the segregation of Pt to the surface, with an oscillatory composition profile with respect to depth, i.e., a Pt-enriched first layer but an M-enriched second layer [26,27]. Whether the top surface is purely Pt depends on the specific crystalline facet [28,29]. In aqueous and electrochemical environments, acid leaching or oxidation of the base metal can also result in a Pt-only exterior, which may be rougher than that obtained through annealing. Such Pt- or bulk-terminated surfaces, even when the bulk compositions are identical, can exhibit different

catalytic and electrocatalytic activity or stability [5,10,25,30-32]. This further complicates the task of assessing how the surface reactivity differs for ordered vs. disordered Pt-M alloys.

While crystalline phase represents a possible way to tune catalytic activity, there is evidently a lack of fundamental understanding of how and why ordered and disordered Pt-M alloys differ catalytically. To shed light on the catalytic properties of disordered Pt-M alloys and identify potential opportunities for disordered alloys in heterogeneous catalysis and electrocatalysis, we use Pt-Ni as an example to assess three different theoretical methods for modeling disordered alloys: Virtual Crystal Approximation (VCA), Korringa–Kohn–Rostoker Coherent Potential Approximation (KKR-CPA), and large explicit supercells generated using a new method, Super-Cell Random Approximates (SCRAPs) [33], which provides far better approximation to complete randomness than simple randomized elemental assignments do because the latter does not prevent the emergence of local order. Notably, Pt-Ni type systems (e.g., Pt-Ni, Pt-Co, Pt-Fe, and Pd-Fe) have been well-studied using KKR (ordered) and KKR-CPA (partially and fully disordered) [34,35]. We compare and contrast bulk crystalline and electronic structures, as well as hydrogen adsorption on bulk-terminated and Pt monolayer (Pt_{ML}) terminated surfaces, for the ordered vs. corresponding disordered alloys. A further motivation for this work stems from a dearth of literature on how interpolative models like the VCA that do not address disorder directly compare to explicit representations of disordered alloys with regard to modeling of surface adsorption. We do not consider adsorbate-induced surface segregation in this work, which primarily occurs at elevated temperatures [36].

Methods

Periodic, spin-polarized density functional theory (DFT) calculations were performed using the

Perdew, Burke, and Ernzerhof generalized gradient functional (GGA-PBE) [37] in two different ways. In one approach, the Kohn-Sham valence states were expanded in a plane-wave basis using Quantum ESPRESSO [38,39]. The atomic potentials were described by optimized norm-conserving Vanderbilt pseudopotentials [40]. The electronic states were expanded up to 100 Ry and smeared with a width of 0.02 Ry using the Marzari-Vanderbilt approach [41]. Electronic convergence criterion was 10^{-6} Ry. The other approach is the all-electron KKR-CPA. The KKR method is a Green's function method for calculating electronic structure and total energy [42-44]. The CPA is a mean-field theory method for calculating the configurationally averaged Green's function for substitutionally disordered alloys [44-47], and when Friedel screening in metals is included, it is highly accurate in comparing ordered and disordered alloys [48]. The atomic potentials were modeled within the atomic sphere approximation (ASA) [49], supplemented by a variationally optimized potential energy zero resulting in formation energies matching full potential results [50]. The valence states were expanded in a spherical harmonic basis that included angular momentum up to l_{max}=6. The Green's function (and hence site-decomposed densities) for each system was found using a semi-circular Gauss-Chebyshev contour integration with 20 complex energy points.

All ordered and disordered alloys in this study were modeled in *fcc* structures. The ordered Ni_3Pt and $PtNi_3$ phases were modeled in the $L1_2$ structure, the ordered PtNi phase in the $L1_0$ structure but with c=a, and the disordered Pt-Ni phases along with the pure elements in the A1 structure. Three different approaches were used to model the disordered Pt-Ni phases: the VCA [51], which generates a linearly interpolated composite potential for a given composition based on the elemental potentials but does not reflect chemical disorder; the KKR-CPA electronic structure method with proper configurational averaging; and a large 108-atom

SCRAPs supercell for each of the following compositions, $Pt_{27}Ni_{81}$, $Pt_{54}Ni_{54}$, $Pt_{81}Ni_{27}$, and $Pt_{92}Ni_{16}$, representing the disordered alloys of $Pt_{0.25}Ni_{0.75}$, $Pt_{0.5}Ni_{0.5}$, $Pt_{0.75}Ni_{0.25}$, and $Pt_{0.85}Ni_{0.15}$, respectively. While no finite supercell could be a unique representation of a given disordered Pt-Ni phase, they were generated using a hybrid Cuckoo Search algorithm [52] with combinatorially optimized atomic point and pair probabilities to ensure an configuration with zero short-range order for up to three nearest-neighbor shells at every atomic site.

For the plane-wave approach, Brillouin zone integration was done on a 24×24×24 Monkhorst-Pack (MP) k-point mesh [53] for the one-atom bulk unit cells of monometallic Ni and Pt and disordered Pt-Ni phases; a 16×16×16 MP k-point mesh for the four-atom bulk unit cells of ordered $PtNi_3$, PtNi, and Pt_3Ni phases; and a 3×3×3 MP k-point mesh for the 108-atom supercells. The Green's function approaches singularity as the energy points approach the Fermi level (ε_F). To treat this case, two MP k-point meshes were used with the KKR-CPA. For energy points with an imaginary part greater than 0.250 Ry a 12×12×12 MP k-point mesh was used, and for energy points with an imaginary part less than 0.250 Ry (i.e., in the neighborhood of ε_F) an 18×18×18 MP k-point mesh was used. These parameters were determined to provide an accuracy of a 10^{-5} Ry in the total energy.

The adsorption of atomic H was modeled on 4-layer slabs exhibiting the (111) facet for all metals and alloys considered in this study (all of which having *fcc* lattices). Pt_{ML}-terminated slabs were created by replacing the top layer of the corresponding bulk-terminated slabs with a pure Pt layer, for which x_{Pt} refers to the corresponding bulk-terminated slabs. Periodic slabs in the z direction were separated by 10~16 Å of vacuum. Adsorption at 1/4 ML was modeled with one H atom per (2×2) surface unit cell. Adsorption at 1 ML was modeled with four H atoms per (2×2) surface unit cell for the ordered phases, one H atom per (1×1) surface unit cell for the

disordered alloys in the VCA, or 36 H atoms per (6×6) surface unit cell cut from the large bulk unit cells approximating the disordered alloys. The surface Brillouin zone was sampled on a 16×16×1 MP k-point mesh for the (1×1) and (2×2) surface unit cells, or on a 2×2×1 MP k-point mesh for the (6×6) surface unit cells.

All metals atoms in the top two layers and all adsorbed H atoms were fully relaxed, while metal atoms in the bottom two layers were fixed at bulk positions. Convergence criteria for geometry optimization were 10^{-6} Ry and 10^{-3} Ry/bohr, respectively. The average adsorption energy of atomic H was calculated as:

$$\Delta E_{ads} = (E_{tot} - E_{slab} - n \cdot E_H) / n \quad (1)$$

where E_{tot}, E_{slab} and E_H are the calculated total energies of the surface with adsorbed H, the clean surface without any adsorbate, and an H atom in the gas phase, respectively, and n is the number of H atoms in a surface unit cell. The gas phase H atom and H_2 in gas phase were calculated in $(20\ \text{bohr})^3$ simulation cells. The predicted H_2 bond energy and bond length are 0.334 Ry (4.55 eV) and 1.42 bohr (0.749 Å).

Results and Discussion

Lattice constant

Fig. 1 illustrates the crystal structures used to model the ordered and disordered alloy phases considered in this study. The calculated minimum-energy lattice constants are tabulated in Table 1 and plotted in Fig. 2, along with available experimental values. Experimental lattice constants of disordered Pt-Ni phases are taken from those studies in which alloy samples were melted or annealed at high temperatures and then rapidly quenched.

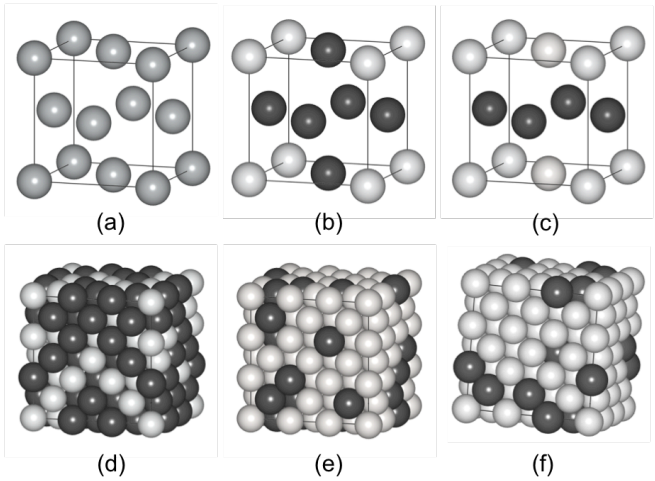

Fig. 1 (a) *fcc* structure for monometallic Ni and Pt, and disordered Pt-Ni phases used in VCA calculations (where Ni and Pt randomly occupy the lattice positions); (b) $L1_2$ structure for ordered Ni_3Pt and $PtNi_3$; (c) hypothetical $L1_0$ structure for PtNi with c=a. Large SCRAPs supercells for (d) $Pt_{27}Ni_{81}$ ($Pt_{81}Ni_{27}$), (e) $Pt_{54}Ni_{54}$, and (f) $Pt_{92}Ni_{16}$. Color code: Pt = light spheres; Ni = dark spheres; Pt and Ni are interchangeable in (b, d) to obtain either the Ni-rich phase or Pt-rich phase.

Table 1 Calculated and experimental lattice constants (in Å) of ordered and disordered Pt-Ni alloys.

x_{Pt}	Ordered	Disordered (VCA)	Disordered (SCRAPs)	Ordered (KKR)	Disordered (KKR-CPA)	Ordered (exp.)	Disordered (exp.)
0.00	3.516	-	-	3.527	-	3.52 [54]	
0.15	-	3.567		-	3.639		
0.25	3.654	3.614	3.657	3.657	3.690	3.646 [55]	
0.33	-	3.655		-	3.729		
0.50	3.775	3.739	3.794	3.780	3.797		3.754 [56], 3.76 [57]
0.66	-	3.825		-	3.853		
0.75	3.875	3.862	3.889	3.881	3.877	3.836 [23], 3.837 [55], 3.84 [57],	3.87 [13]†
0.85	-	3.907	3.923	-	3.913		
1.00	3.967	-	-	3.970	-	3.92 [54]	

† Ordered $PtNi_3$ phase in the $L1_2$ structure has not been confirmed experimentally.

The dependence of lattice constant on composition is generally as expected, i.e. smaller lattice constant with decreasing x_{Pt} due to the smaller atomic radius of Ni than Pt. The lattice constants of the three ordered phases show positive deviation from the linear interpolation between monometallic Ni and Pt that represents Vegard's law. The lattice constants of the disordered A1 phase calculated in the VCA adhere closely to Vegard's law. This is not surprising since the VCA uses atomic potentials that are constructed from linear interpolation of pure elements, which evidently results in linear interpolation of the atomic size among other properties. The VCA results yield A1 phases that are smaller than the ordered phases of the same compositions, which is atypical for metallic alloys except in unusual cases [48].

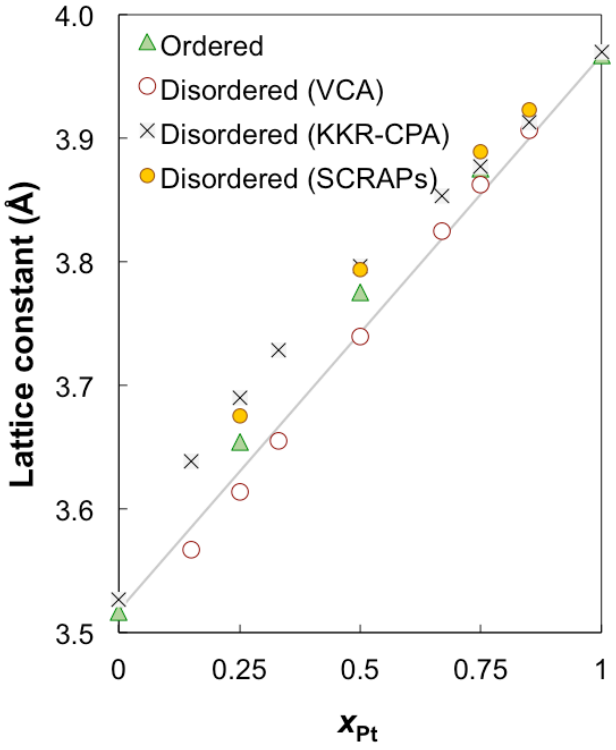

Fig. 2 Calculated lattice constants of Pt-Ni phases plotted against Pt atomic concentration (x_{Pt}). Line connects monometallic Ni and Pt represents Vegard's law.

On the other hand, the lattice constants based on the large supercells are consistently larger than those of the ordered phases by 0.01~0.02 Å, and larger than those of the VCA disordered alloys of the same compositions by 0.03 Å (Pt_3Ni) ~ 0.06 Å ($PtNi_3$) (or 0.7~1.7%), which suggests that linear interpolation of atomic size underestimates the contribution by the larger element (Pt) to the bulk volume. The supercells for A1 $Pt_{0.25}Ni_{0.75}$, $Pt_{0.5}Ni_{0.5}$, and $Pt_{0.75}Ni_{0.25}$ are 0.0705, 0.0745, and 0.0592 eV per atom higher in energy than the corresponding ordered $PtNi_3$, PtNi, and Pt_3Ni phases, consistent with the expectation that the disordered alloys should be energetically less stable than the corresponding ordered phases, at least when an

ordered phase ($PtNi_3$) exists. Notably, for a miscible alloy, the energy difference (δE) between the ordered and disordered alloys has been shown to be an excellent estimate for the order-disorder transition critical temperature T_c [35,58], i.e.,

$$T_c \approx \frac{\delta E}{k_B} \tag{2}$$

which reflects the fact that such a transition corresponds to the excitation of exactly one additional degree of freedom, i.e. $\Delta S = k_B$. For $PtNi_3$ - $Pt_{0.25}Ni_{0.75}$ transition Eqn. 2 yields T_c = 545 ºC, compared to the observed maximum T_c of 580 ºC [12].

The lattice constants predicted by KKR-CPA for monometallic Ni and Pt and the ordered Pt-Ni phases exceed the plane wave results by no more than 0.3%, so below we will omit the KKR-CPA results for the ordered phases from discussion. The lattice constants of the disordered alloys predicted by KKR-CPA also deviate positively from linear interpolation between the pure elements. They agree well with those predicted by the large supercells, not the VCA (Fig. 2). The predicted lattice constants can be fit to third order polynomials: $0.082 \cdot x_{Pt}^3 - 0.315\ x_{Pt}^2 + 0.676\ x_{Pt} + 3.524$ (SCRAPs), or $0.371\ x_{Pt}^3 - 0.748\ x_{Pt}^2 + 0.819\ x_{Pt} + 3.528$ (KKR-CPA), with $R^2 = 1.000$ for both.

There is a lack of consistency in the experimental literature on the lattice constants of ordered vs. disordered Pt-Ni alloys. There are no comparable data for disordered $Pt_{0.25}Ni_{0.75}$ to ordered $PtNi_3$, and while the actual ordered PtNi forms in the *fct* $L1_0$ structure, an ordered phase may not exist for Pt_3Ni. GGA-PBE is known to over-predict the lattice constants of metals on average by 1.0% [59], which complicates comparison with experimental values to resolve such

minute differences. Our results (Table 1) show that while the GGA-PBE lattice constant of Ni is 0.06% too small while that of Pt is over-predicted by 1.2%. If we assume that the lattice constant of $Pt_{0.75}Ni_{0.25}$ has similarly been over-predicted by 1.2%, then the VCA, KKR-CPA, and large supercell would predict 3.816, 3.834, and 3.842 Å, respectively for $Pt_{0.75}Ni_{0.25}$, which we take to be a disordered alloy. Thus the KKR-CPA and SCRAPs are more reliable than VCA for predicting the lattice constant of disordered Pt-Ni phases, as shown in $Pt_{0.75}Ni_{0.25}$.

Bulk electronic structure

Next we examine the electronic structure of Pt-Ni phases. Understanding how the electronic structure of ordered and disordered Pt-Ni phases differ theoretically may offer a way to distinguish them spectroscopically [60-62] when other measures such as lattice size are inconclusive. We present and compare the projected density of states (DOS) for ordered $PtNi_3$, PtNi, and Pt_3Ni and disordered $Pt_{0.25}Ni_{0.75}$, $Pt_{0.5}Ni_{0.5}$, and $Pt_{0.75}Ni_{0.25}$ in Fig. 3. The DOS of monometallic Pt and Ni is shown in Fig. S1 in Supporting Information (SI) for comparison.

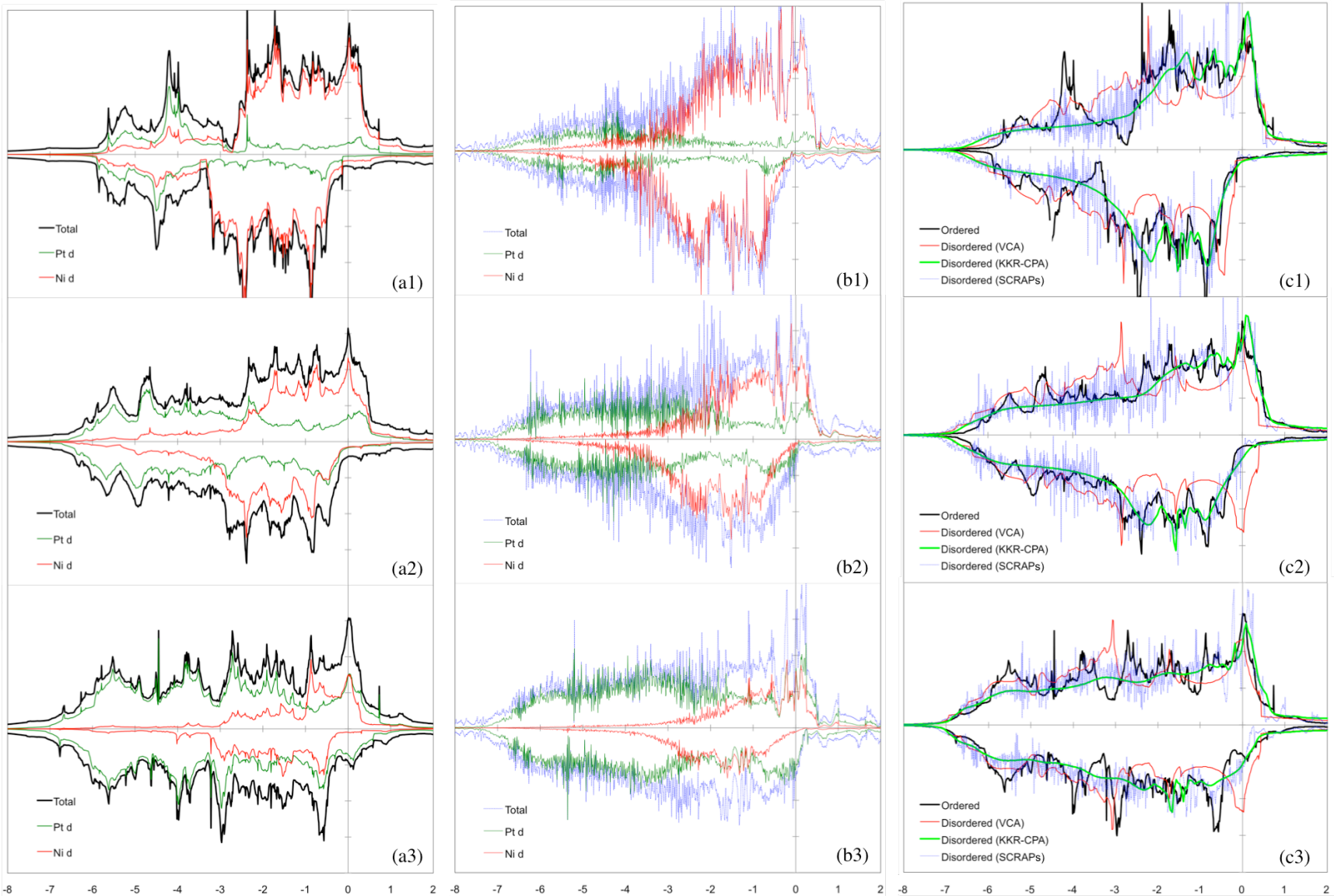
Total
Pt d
Ni d
(a1)
(a2)
(a3)
(b1)
(b2)
(b3)
Ordered
Disordered (VCA)
Disordered (KKR-CPA)
Disordered (SCRAPs)
(c1)
(c2)
(c3)
-8 -7 -6 -5 -4 -3 -2 -1 0 1 2

Fig. 3 Total DOS (*spd* on all atoms in unit cell) and atom-decomposed *d* DOS (on all Pt or Ni atoms in unit cell) normalized by total number of atoms in unit cell for (a1-a3) ordered $PtNi_3$, PtNi, and Pt_3Ni, and (b1-b3) disordered $Pt_{0.25}Ni_{0.75}$, $Pt_{0.5}Ni_{0.5}$, and $Pt_{0.75}Ni_{0.25}$ calculated using the large supercells. (c1-c3) Comparison of the total *d* DOS (on all Pt and Ni atoms in unit cell) of the three disordered alloys calculated from VCA, KKR-CPA, and SCRAPs approaches.

In Fig. 3 (a1-a3) and (b1-b3) we plot the total DOS and atom-decomposed *d* DOS for ordered $PtNi_3$, PtNi, and Pt_3Ni, and the disordered alloys of the same compositions based on the large supercells. Many similarities can be seen between how the total DOS and the Pt and Ni *d* DOS are distributed in Fig. 3a and 3b. Above −3 eV, Ni contributes strongly to the total DOS, and vice versa for Pt below −3 eV. Thus there is a substantial contribution by Ni at and immediately below ε_F even for Pt_3Ni. Coupling of Pt 5*d* states and Ni 3*d* states is visible within −1 eV of ε_F for all three ordered phases, while it is primarily seen in the spin-up channel for disordered $Pt_{0.5}Ni_{0.5}$ and $Pt_{0.75}Ni_{0.25}$. From Fig. 3c, it is clear that the large supercells produce reasonable average electronic structures in agreement with KKR-CPA for the disordered alloys.

The center (ε_d), or first moment, of the Ni 3*d* band up-shifts (Table 2) with increasing x_{Pt}, and at the same time the magnetic moment on Ni atoms increases well above that of bulk Ni. Pinski et al. identified the origin of Hume-Rothery's 15% size effect rule for stability of solid solution phases to be the electronic manifestation of atomic size given by the elemental bandwidths upon alloying (e.g., the Ni bandwidth is narrowed on the larger lattice constant of the

alloy whereas the Pt bandwidth is increased; see Table S1 in SI). This interplay leads to Pt- and Ni-hybridized t_{2g} states (which appear in –6 ~ –3 eV in Fig. 3 (a1-c1)), which at larger lattice constants (or here at larger x_{Pt}) are not supported and lose stability [34,63]. These t_{2g} states are further enhances upon ordering, as seen in Fig. 3c1, for example. Echoing this, Kitchin and co-workers recently reported that the electronic structure of single atoms of reactive metals embedded in coinage metals [64] is often atom-like, which is attributable to electronic isolation of the impurity atom in the host lattice. However, in the case of Pt-Ni, the Ni 3*d* band does not narrow significantly or exhibit sharper features with increasing x_{Pt}, nor does the Pt 5*d* band with decreasing x_{Pt}. This reflects effective coupling of the Pt and Ni *d* states (due to hybridization) despite the fact that the lattice constant of Pt is ca. 13% larger than that of Ni, which would impose a significant effective tensile strain on Ni atoms in a primarily Pt lattice [34,64]. All of these features are consistent with the valence-band photoemission spectra of Pt-Ni disordered alloys obtained by Nahm et al. [65]. Overall, there are few distinct qualitative differences between Fig. 3a and 3b, suggesting it may be difficult to resolve order vs. disorder in Pt-Ni alloys spectroscopically.

Table 2 Electronic properties of bulk monometallic Pt and Ni, ordered $PtNi_3$, PtNi, and Pt_3Ni, and disordered $Pt_{0.25}Ni_{0.75}$, $Pt_{0.5}Ni_{0.5}$, $Pt_{0.75}Ni_{0.25}$, and $Pt_{0.85}Ni_{0.15}$: *d* band center (ε_d, in eV, relative to ε_F) and average magnetic moment (in μ_B/atom).

	ordered		disordered (VCA)		disordered (KKR-CPA)		disordered (SCRAPs)	
	ε_d	mag. mom.	ε_d	mag. mom.	ε_d	mag. mom.	ε_d	mag. mom.
Ni	−1.29	0.66	-	-	−1.43[†]	0.70	-	-
$PtNi_3$ or	−1.61	0.66	−1.89	0.64	−1.66	0.68	−1.62	0.64
$Pt_{0.25}Ni_{0.75}$	−2.89 (Pt)	0.38 (Pt)			−3.18 (Pt)	0.30 (Pt)	−3.11 (Pt)	0.34 (Pt)
	−1.18 (Ni)	0.80 (Ni)			−1.20 (Ni)	0.80 (Ni)	−1.13 (Ni)	0.78 (Ni)
PtNi or	−1.92	0.58	−2.45	0.01	−1.98	0.60	−1.95	0.56
$Pt_{0.5}Ni_{0.5}$	−2.75 (Pt)	0.37 (Pt)			−2.95 (Pt)	0.30 (Pt)	−2.91 (Pt)	0.32 (Pt)
	−1.08 (Ni)	0.84 (Ni)			−1.08 (Ni)	0.90 (Ni)	−0.99 (Ni)	0.85 (Ni)
Pt_3Ni or	−2.36	0.33	−2.62	0.01	−2.37	0.43	−2.30	0.41
$Pt_{0.75}Ni_{0.25}$	−2.81 (Pt)	0.18 (Pt)			−2.85 (Pt)	0.25 (Pt)	−2.77 (Pt)	0.26 (Pt)
	−0.99 (Ni)	0.82 (Ni)			−1.01 (Ni)	0.97 (Ni)	−0.89 (Ni)	0.92 (Ni)
$Pt_{0.85}Ni_{0.15}$	-	-	-2.66	0.00	−2.50	0.33	−2.47	0.30
					−2.79 (Pt)	0.22 (Pt)	−2.75 (Pt)	0.20 (Pt)
					−0.97 (Ni)	1.01 (Ni)	−0.87 (Ni)	0.92 (Ni)
Pt	−2.71	-	-	-	−2.74[†]	-	-	-

For magnetic phases ε_d of the spin-up channel is reported. The corresponding width of *d* band (W_d) is listed in Table S1.

[†]Ordered phase using KKR only.

Previous DFT-GGA calculations reported 0.59, 0.58, and 0.30 μ_B/atom for Ni and ordered $PtNi_3$ and Pt_3Ni [66], with which our results (Table 2) agree closely. The different disorder models produce different predictions for the disordered alloys. The VCA indicates disordered $Pt_{0.5}Ni_{0.5}$, $Pt_{0.75}Ni_{0.25}$, and $Pt_{0.85}Ni_{0.15}$ to be essentially non-magnetic (Table 2), i.e., the magnetic moment is quenched at x_{Pt} as low as 0.5. It can be seen in Fig. 3c2 and 3c3 that the spin-up and spin-down DOS of disordered $Pt_{0.5}Ni_{0.5}$ and $Pt_{0.75}Ni_{0.25}$ are symmetric at ε_F according to VCA. Comparison of the VCA results (Fig. 3c) with monometallic Pt (Fig. S1) suggests that

the lack of magnetism is due to greater presence of the Pt DOS within ca. −2 eV of ε_F according to VCA than is predicted by the large unit cells.

On the other hand, the large supercells and KKR-CPA approaches predict the disordered $Pt_{0.25}Ni_{0.75}$, $Pt_{0.5}Ni_{0.5}$, and $Pt_{0.75}Ni_{0.25}$ phases to be ferromagnetic with average magnetic moments that are close to those of the corresponding ordered phases. In particular, a noticeable moment remains on Pt up to x_{Pt}=0.75. KKR-CPA indicates that the ferromagnetic state is 1.51×10^{-2} eV/atom more stable than the non-magnetic phase at x_{Pt}=0.75, and the difference drops below 10^{-4} eV/atom at x_{Pt}=0.85. Similarly, the large supercells indicate the ferromagnetic state to be 1.86×10^{-2} and 1.05×10^{-2} eV/atom more stable than the non-magnetic phase at x_{Pt}=0.75 and 0.85, respectively. While we still report the ferromagnetic results in Table 2, it is clear that the magnetic moment is essentially quenched at x_{Pt}=0.85.

Experimentally Parra et al. reported that disordered Pt-Ni phases are overall ferromagnetic, with the average magnetic moment decreasing with increasing x_{Pt}, down to ca. 0.1 μ_B/atom at x_{Pt}=0.57, which is the maximum Pt concentration that they investigated using neutron diffuse scattering [56]. The average moment decreases more quickly with composition than that predicted by the large supercells and KKR-CPA approaches. We attribute this discrepancy to the fact that the theoretical calculations yield local moments and do not reflect the heterogeneity of spin orientation that can exist in macroscopic domains. In any case, the large supercell and KKR-CPA approaches agree with available experimental results that the disordered alloys are ferromagnetic up to at least x_{Pt}=0.5.

Another important characteristic of the electronic structure of transition metals is ε_d, which is also reported in Table 2 and plotted visually as a function of atomic composition in Fig. S2. The ε_d of Pt and Ni in the literature are typically reported for certain facets (e.g. Pt(111): −2.3~−2.7 eV; Ni(111): −1.3~−1.6 eV) [60,67-72]. The ε_d of bulk Pt is reported by Hammer et al. to be −2.75 eV [73], with which our result is in close agreement. The ε_d of the three disordered alloys modeled using the large supercells and KKR-CPA tracks the ε_d of the correspondingly ordered phases closely, and varies nearly linearly with composition. On the other hand, the ε_d of the same three disordered alloys diverge from linearity with respect to composition according to the VCA. Whether ε_d vs. composition exhibits linearity in disordered Pt-Ni alloys may be another experimentally verifiable aspect that can help establish which disorder model is more accurate. Note that linear variation of ε_d with x_{Pt} does not necessarily imply that reactivity toward H adsorption energy varies linearly with x_{Pt}, as discussed below.

Atomic H adsorption on bulk-terminated surfaces

Next, we investigate the site preference for atomic H adsorbed on the (111) facets of monometallic Ni and Pt and the ordered alloys. The surface models are illustrated in Fig. 5. The calculated adsorption energies (ΔE_{ads}) are reported in Table 3. All slab models are constructed at the corresponding bulk lattice constants as reported above. We mainly focus on the compositions of $PtNi_3$, PtNi, and Pt_3Ni to facilitate comparison between ordered and disordered Pt-Ni phases. H adsorption on additional intermediate disordered compositions is

calculated in the VCA only.

At 1/4 ML coverage, atomic H prefers the *fcc* sites to *hcp* sites on all the ordered surfaces considered in this study. ΔE_{ads} is calculated to be −2.82 eV on Ni(111) and −2.75 eV on Pt(111), which agree closely with previous DFT results calculated using the GGA-PBE and GGA-PW91 functionals, whereas those based on GGA-PRBE are less exothermic by 0.1~0.2 eV (Table 3). The potential energy surface for H appears to be more corrugated on Ni(111) than on Pt(111). The experimentally measured heats of H_2 dissociative adsorption on Ni(111) and Pt(111) fall between the PBE/PW91 and RPBE values.

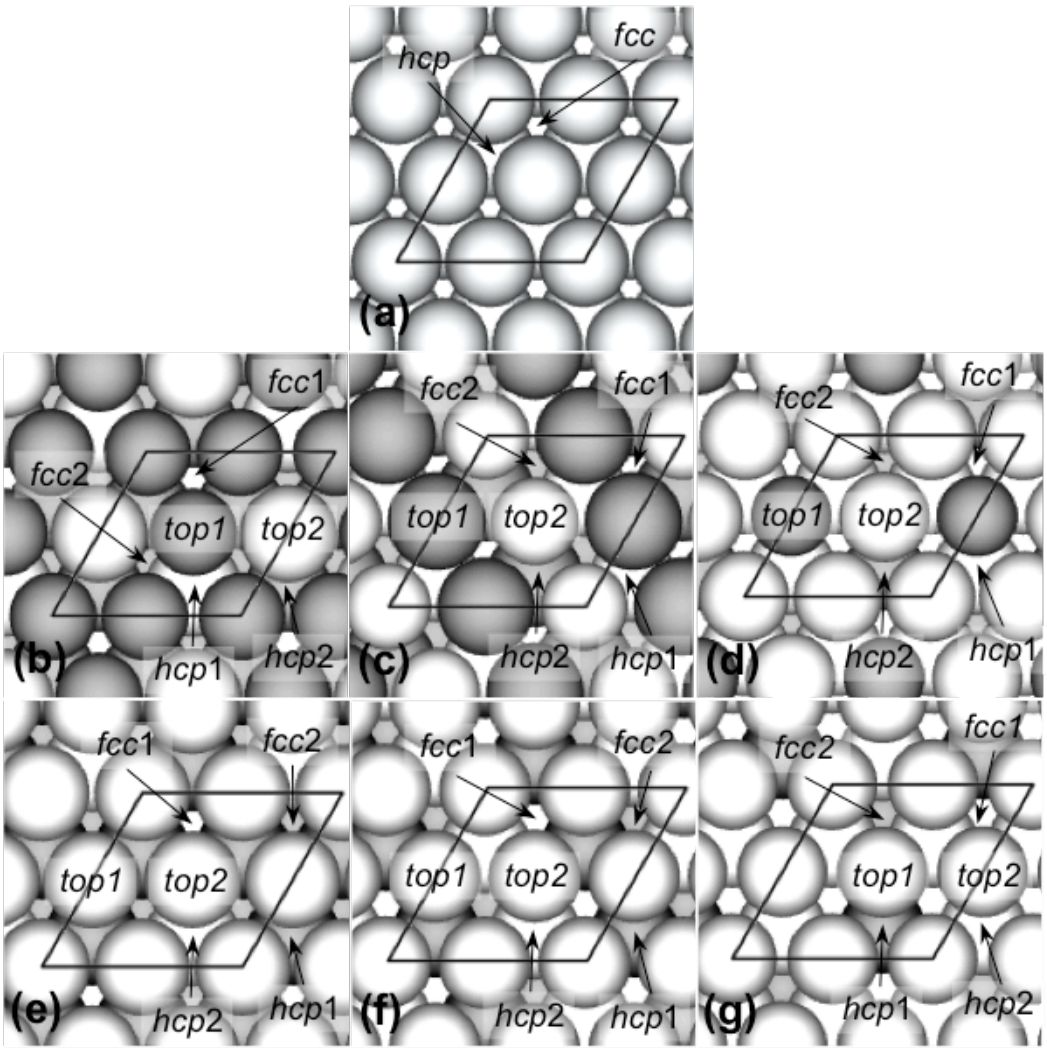

Fig. 5 Top views of the (111) surface models for: 1) monometallic Ni and Pt, and disordered Pt-Ni in the A1 phase used in VCA calculations; (b) ordered $PtNi_3$; (c) ordered PtNi; (d) ordered Pt_3Ni; (e) Pt_{ML} on ordered $PtNi_3$; (f) Pt_{ML} on ordered PtNi; (g) Pt_{ML} on ordered Pt_3Ni. Color code: Pt = light spheres; Ni = dark spheres. High-symmetry adsorption sites considered in this study are labeled. The (2×2) surface unit cells are outlined.

Table 3 Adsorption energy of atomic H (ΔE_{ads}) on the (111) facet of Ni, Pt, and ordered Pt-Ni alloys, in comparison with literature DFT and experimental values.

	Ni	$PtNi_3$	PtNi	Pt_3Ni	Pt	Pt_{ML}/Ni	Pt_{ML}/$PtNi_3$	Pt_{ML}/PtNi	Pt_{ML}/Pt_3Ni
fcc / *fcc*1	−2.82 *−0.55*	−2.80 *−0.53*	−2.75 *−0.48*	−2.72 *−0.45*	−2.75 *−0.48*	−2.24 *+0.03*	−2.45 (*br*) *−0.18*	−2.57 (*br*) *−0.30*	−2.65 *−0.38*
*fcc*2		−2.74	−2.70	−2.67			−2.41 (*br*)	−2.47	−2.56
hcp / *hcp*1	−2.81	−2.69	−2.69	−2.67	−2.70	−2.24	−2.45 (*br*)	−2.47	−2.54
*hcp*2		−2.75	−2.71	−2.65			−2.41 (*br*)	−2.57 (*br*)	−2.62
top / *top1*	−2.23	(*fcc*1)	(*fcc*1)	−2.18	−2.73	−2.50	−2.29	−2.41	−2.55
top2		−2.54	−2.58	−2.64			−2.45	−2.59	−2.77
fcc[†]	−2.80	−2.73	−2.69	−2.65	−2.67	−2.08 (*top*)	−2.27 (*top*)	−2.41 (*top*)	−2.52 (*top*)
GGA-PW91	−2.83 [71], −2.84 [74], −2.89 [75,76], −2.96 [70], *−0.53*[¶] [77], *−0.55* [78]			−2.59 [70]	−2.71[§] [79], −2.74 [80], −2.75 [71], −2.76 [74], *−0.49* [81,78] *−0.43*[†] [82]		*−0.11* [81]		*−0.37* [81]
GGA-PBE	−2.94 [83], *−0.54* [78], *−0.60* [84]			*−0.54* [84]	*−0.41* [78], *−0.45* [84], *−0.53, −0.46*[†] [85]				
GGA-RPBE	−2.72 [75], *−0.41* [78]				−2.57 [80], *−0.34* [78]				
Exp.	*−0.48* [86], *−0.49* [87]				*−0.40* [88], *−0.37* [74]				

DFT ΔE_{ads} is calculated at 1/4 ML except where noted: [†]1 ML; [¶]1/12 ML; [§]1/9 ML. Values in italics are with respect to molecular H_2 instead of H. To convert a ΔE_{ads} calculated with respect to H onto the H_2 basis, add half of the H_2 bond energy (+2.27 eV) to the ΔE_{ads}. The literature DFT data cited are those for atomic H in the *fcc* site when site preference is reported. Change of site upon optimization is

On each of the three bulk-terminated *ordered* Pt-Ni alloy surfaces, two distinct *fcc* sites and two distinct *hcp* sites exist due to different atomic compositions of the three metal atom ensemble that surrounds each threefold site. Within each type of site, we label the site with the greater number of Ni atoms in the ensemble "1" and the other site "2". The most stable site is invariably the *fcc*1 site, consistent with previous findings on $Pt_3M(111)$ surfaces [84,69]. ΔE_{ads} generally becomes less negative with greater x_{Pt} although ordered Pt_3Ni is slightly less reactive than monometallic Pt. Measured or calculated ΔE_{ads} on bulk-terminated ordered Pt-Ni alloy surfaces are scarce in the literature. The calculated ΔE_{ads} reported by e.g. Shin et al. and Pillay et al. for atomic H at 1/4 ML on $Pt_3Ni(111)$ differ from our result by ca. 0.1 eV [70,84].

A disordered alloy surface presents a myriad of adsorption sites that are compositionally distinct to different orders of nearest neighbors, which in turn induce subtly different interactions amongst sites. In the simplest approach, atomic H adsorption on the bulk-terminated ordered and *disordered* Pt-Ni alloy surfaces is compared at 1 ML coverage. The latter is calculated in two ways, on (1×1) surface unit cells in the VCA and on the (6×6) surface unit cells cut from the SCRAPs supercells (shown in Fig. S3, with coordinates listed in the SI). The average ΔE_{ads}, which is perhaps the most direct measure of the overall reactivity of an explicitly represented disordered alloy surface with adsorbate-adsorbate interaction taken into account, is compared with a single value for ΔE_{ads} produced by VCA on all identical *fcc* sites. The average ΔE_{ads} at 1 ML on the various surfaces are plotted in Fig. 6.

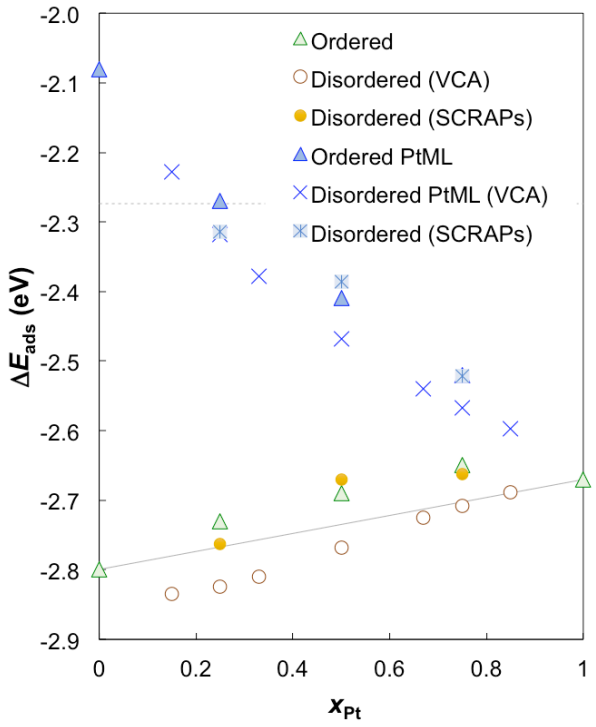

Fig. 6 Average adsorption energy (ΔE_{ads}) for atomic H at 1 ML coverage on the (111) facet of monometallic Ni and Pt, and bulk-terminated and Pt_{ML}-terminated ordered and disordered Pt-Ni alloys, plotted against Pt atomic concentration (x_{Pt}). The negative of half of the H_2 bond energy is indicated (−2.27 eV). Solid line connecting monometallic Ni and Pt is a guide to the eye only.

At 1 ML, atomic H preferentially occupies the *fcc* site on Ni(111), Pt(111), and the three bulk-terminated ordered Pt-Ni(111) facets. We note that the *top* site may be occupied at higher still coverage [89]. The average ΔE_{ads} at 1 ML exhibits the same trend as ΔE_{ads} at 1/4 ML and are less negative by less than 0.1 eV, at −2.73, −2.69, and −2.65 eV on $Pt_{ML}/PtNi_3(111)$, $Pt_{ML}/PtNi(111)$, $Pt_{ML}/Pt_3Ni(111)$, respectively. ΔE_{ads} on the three ordered alloy surfaces and

ΔE_{ads} on the (6×6) disordered surfaces (with H atoms occupying all *fcc* sites) both lie slightly positive of linear interpolation between ΔE_{ads} of monometallic Ni(111) and Pt(111). The two sets of values are practically identical within DFT accuracy. The VCA results, on the other hand, deviate increasingly negatively from the linear trend with decreasing x_{Pt}, forming a minimum around x_{Pt}=0.15. The close parallel between ΔE_{ads} on the (111) facets of the ordered and disordered alloys of the same composition appears reasonable and is reflective of their chemical similarity, whereas the deviation of the VCA results highlights its failure to correctly represent either the local or the average electronic structure of alloys.

To our knowledge, there has been no experimental study in the literature that investigates how the adsorption of common species such as atomic H systematically varies with composition on bulk-terminated ordered or disordered Pt-Ni alloy surfaces. Nonlinear variations of adsorption energy with composition have been reported by Zhang et al. for oxygen on several Pd-based random alloys, using a model construction approach that does not check for short-range order [90].

Atomic H adsorption on Pt_{ML}-terminated surfaces

As mentioned above, a Pt-only exterior can form on Pt-M alloys due to processes such as annealing followed by slow cooling or acid leaching. Therefore adsorption on a Pt-terminated surface is an integral aspect of Pt-M alloy surface reactivity. We use a simple model, constructed by replacing the top metal layer of an alloy slab with a layer of Pt, to represent such

surfaces and calculate the adsorption of atomic H thereon.

At 1/4 ML, ΔE_{ads} on Pt_{ML}-terminated *ordered* $PtNi_3(111)$ and $Pt_3Ni(111)$ that we have calculated are comparable to what is reported by Su et al. [81], and that on $Pt_{ML}/PtNi(111)$ falls in between. On $Pt_{ML}/PtNi_3(111)$, atomic H is preferentially located on the twofold *bridge* site between adjacent *fcc*1 and *hcp*1 sites, and on the *bridge* site between adjacent *fcc*2 and *hcp*2 sites, instead of the threefold sites. The same phenomenon is seen on $Pt_{ML}/PtNi(111)$ where H on the *fcc*1 or *hcp*2 site moves to the bridge site between them upon optimization.

To compare Pt_{ML}-terminated ordered and disordered alloy surfaces, we have taken the same approach as above and modeled and calculated ΔE_{ads} of atomic H at 1 ML coverage. At 1 ML, atomic H prefers to be located on the *top* site to the *fcc* site by −0.08, −0.04, and less than −0.01 eV per H on $Pt_{ML}/PtNi_3(111)$, $Pt_{ML}/PtNi(111)$, and $Pt_{ML}/Pt_3Ni(111)$, respectively. The average ΔE_{ads} is 0.1~0.2 eV per H less exothermic than at 1/4 ML, at −2.27, −2.41, and −2.52 eV on these three surfaces, respectively. In comparison, according to VCA atomic H similarly prefers the *top* site to *fcc* site at 1 ML on $Pt_{ML}/Pt_{0.25}Ni_{0.75}(111)$, $Pt_{ML}/Pt_{0.5}Ni_{0.5}(111)$, and $Pt_{ML}/Pt_{0.75}Ni_{0.25}(111)$, with average ΔE_{ads} of −2.32, −2.47, and −2.57 eV, respectively, which, unlike in the bulk-terminated case, trend closely with the average ΔE_{ads} on the corresponding Pt_{ML}-terminated ordered alloys of the same compositions (Fig. 6). This is reasonable due to screening of the underlying metal atoms by the Pt_{ML}. A linear trend of ΔE_{ads} for several adsorbates with respect to composition on Pt_{ML}/Pd_xAu_{1-x} random alloys has been reported before by Zhang et al. [91]. When we examined the adsorption of 1 ML of atomic H adsorbed on top

sites on the three (6×6) Pt_{ML}-terminated disordered surfaces, the average ΔE_{ads} was found to be similar to that on the corresponding Pt_{ML}-terminated ordered surfaces (Fig. 6). However, the energy of the system can be lowered further through H-induced surface reconstruction in $Pt_{ML}/Pt_{0.25}Ni_{0.75}(111)$ and $Pt_{ML}/Pt_{0.5}Ni_{0.5}(111)$, by -1.73 and -0.61 eV respectively (per simulation cell; see Fig. S4 for the reconstructed (6×6) $Pt_{ML}/Pt_{0.25}Ni_{0.75}(111)$ and $Pt_{ML}/Pt_{0.5}Ni_{0.5}(111)$ surfaces). We attribute the reconstruction to increased compressive strain in the Pt_{ML} when x_{Pt} in the bulk decreases, which makes a pseudomorphic Pt_{ML} increasingly less stable for $x_{Pt} \leq 0.5$. In such a case, if a monolayer equivalent of Pt is deposited on a Pt-Ni alloy, 3D island formation should be expected to occur some extent [92].

Overall, Fig. 6 highlights the key trends for ΔE_{ads} on the Pt_{ML} surfaces: Instead of becoming more exothermic with increasing Ni content as on the bulk-terminated surfaces, ΔE_{ads} becomes *less* exothermic. Here the strain effects are dominant as the Pt_{ML} becomes increasingly compressed with decreasing lattice size as x_{Pt} decreases (cf. Fig. 2), while the ligand effects are largely screened out by the Pt_{ML} [8,67,68]. Below x_{Pt}~0.25 the ΔE_{ads} of atomic H on Pt_{ML}-terminated Pt-Ni alloy surfaces become less exothermic than half of the H_2 bond energy, indicating the reactivity of such Pt_{ML} surfaces can no longer sustain the adsorption of a full ML of atomic H.

d-band model

The Hammer-Nørskov *d*-band model postulates that ΔE_{ads} on metal surfaces is determined by the

center of the *d* band (ε_d), the coupling matrix element (V) between the adsorbate states and the *d* band, and the filling of the *d* band (f) [73]. A common interpretation of the *d*-band model is that ΔE_{ads} should vary linearly with ε_d, which appears to be true in this case (Fig. 7a). In fact, the original model postulates that ΔE_{ads} is the sum of ΔE_{sp} and ΔE_d. The H *s* states first interact with the metal *sp* band and form a new resonance. This interaction is stabilizing and relatively constant. For adsorption on the (111) facet of Al, an *fcc* metal that has only *sp* electrons, the renormalized H *s* states peak at ε_A=−6.6 eV. Xin et al. have estimated an up-shift of 2.5 eV in DOS on Pt(111) vs. Al(111) due to difference in *sp* electron density [93]. Thus ε_A is set to be −4.1 eV. The renormalized H *s* states then interact with the metal *d* band, which is repulsive:

$$\Delta E_d = -2(1-f)\frac{V^2}{|\varepsilon_d - \varepsilon_A|} + 2(1+f)\alpha V^2 \quad (3)$$

Both V and ε_d have been shown to be dependent on *d* orbital size to various powers [93-95]. Thus, we postulate $V^2=(\varepsilon_d^2)^\beta$. We limit our analysis to the surfaces and sites composed purely of Pt so that f is taken as being constant (0.9). α is set to be 0.3 [73]. This leaves ΔE_{sp} and β as adjustable parameters, which are obtained by minimizing the root-mean-square differences between the DFT-calculated ΔE_{ads} and the model predictions (Fig. 7b). The results reveal that the attractive first term in Eqn. 3 is less than 20% in magnitude of the repulsive second term. β takes on a positive fractional value, which makes the adsorption of H stronger with increasing (i.e., less negative) ε_d (cf. Fig. 7a) like many, but not all, common adsorbates on Pt [93,94]. The quantity $\partial\Delta E_{ads}/\partial\varepsilon_d$ is evaluated to become increasingly negative with increasing ε_d, which explains the noticeable curvature when ΔE_{ads} is plotted against ε_d (Fig. 7a).

As a test of the model, we use it to predict the ΔE_{ads} of H on several Pt-terminated disordered Pt-Ni surfaces (Fig. 7b). The model produces very close predictions compared to the DFT values. Thus, although the VCA does not describe the electronic structure of the disordered Pt-Ni phases correctly, the effect of such an electronic structure on the reactivity of a Pt overlayer is nonetheless predicted correctly by the *d*-band model.

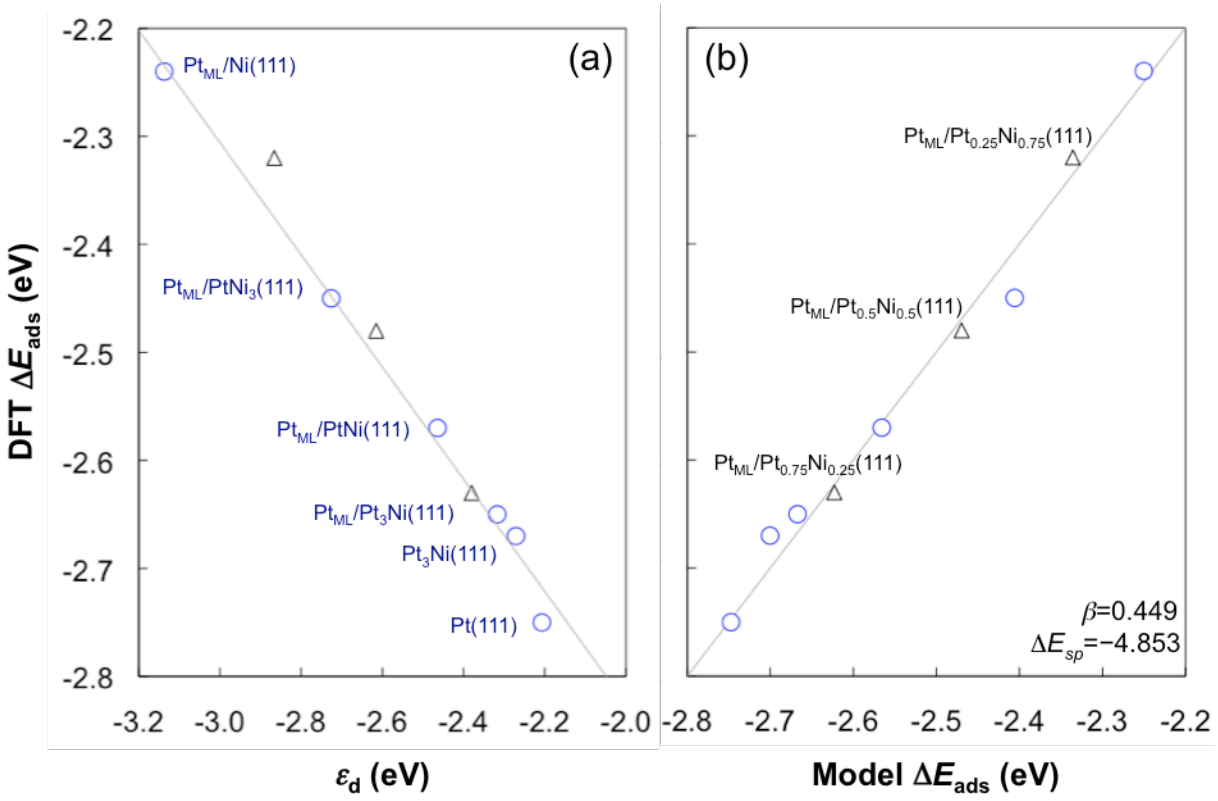

Fig. 7 DFT-calculated ΔE_{ads} of H on Pt surfaces or sites plotted against (a) ε_d (relative to ε_F) and (b) predicted ΔE_{ads} based on the *d*-band model. Line in (a) is linear regression whereas line in (b) indicates parity. The best-fit values for model parameters (based on the circular points) are listed in (b). For pure Pt surfaces, the most negative ΔE_{ads} (Table 2) and the ε_d of the *d* band

of the Pt monolayer are used. For $Pt_3Ni(111)$, the ΔE_{ads} and ε_d associated with the *fcc*2 site are used. For magnetic systems ε_d of the spin-up channel are used. The triangular points are Pt_{ML}-terminated disordered Pt-Ni (111) surfaces as test of the model. All ΔE_{ads} are calculated at 1/4 ML to minimize the effect of adsorbate-adsorbate interaction.

Conclusions

We have showed that DFT-based KKR-CPA, a mean-field method that treats compositional disorder and electronic structure on equal footing, and plane-wave methods using large explicit supercells generated from the SCRAPs approach, produce results that closely agree on both lattice constant and electronic structure for disordered Pt-Ni alloys in the A1 phase across the composition range, and that are in line with the limited experimental evidence available in the literature. The VCA, on the other hand, produces results that qualitatively deviate from the other two methods and experimental data in terms of lattice constant and electronic properties.

We then compare the adsorption energy of atomic H on the (111) facets of ordered vs. disordered Pt-Ni alloys, using large (6×6) surface unit cells cut from the SCRAPs bulk supercells to represent the disordered surfaces. On the basis of the average ΔE_{ads} of H at 1 ML coverage, the chemical reactivity of the three ordered Pt-Ni alloys ($PtNi_3$, PtNi, and Pt_3Ni) is found to be similar to that of disordered Pt-Ni alloys of the same overall compositions (i.e. $Pt_{0.25}Ni_{0.75}$, $Pt_{0.5}Ni_{0.5}$, and $Pt_{0.75}Ni_{0.25}$), on both bulk-terminated and Pt monolayer-terminated surfaces.

ΔE_{ads} of atomic H on Pt-Ni alloys spans across a wide range of ca. 0.7 eV (−2.8 ~ −2.1

eV). Potentially any value in this range is accessible with an appropriate Pt_xNi_{1-y} composition and material synthesis route (i.e. what bulk phase is achieved; whether a Pt skin is formed). Our findings provide an improved basis for understanding the catalytic properties of not only Pt-Ni but other related alloys, which suggest many opportunities in catalysis even with just one pair of metals, particularly in low or mild temperature applications in which the alloy structure is kinetically frozen. They also show by how much the hydrogen adsorption energy could vary with structure and composition on a given binary alloy [11,36,96], potentially resulting in inaccurate interpretation of experimentally measured catalytic activity if these factors are not carefully controlled.

Acknowledgments

We dedicate this article to Professor Manos Mavrikakis in honor of his 2019 Gabor A. Somorjai Award for Creative Research in Catalysis. Modeling and simulation work was supported by the U.S. Department of Energy, Office of Science, Basic Energy Sciences, Catalysis Science Program, under Award No. DE-SC0018408 and was performed at Louisiana State University using high-performance computing resources provided by LSU (hpc.lsu.edu) and by the National Energy Research Scientific Computing Center, an Office of Science User Facility supported by the Office of Science of the U.S. Department of Energy under Contract No. DE-AC02-05CH11231. Computational materials software development was supported by the U.S. Department of Energy, Office of Science, Basic Energy Sciences, Materials Science &

Engineering Division and was done at Ames Laboratory. Ames Laboratory is operated by Iowa State University for the U.S. Department of Energy under Contract No. DE-AC02-07CH11358.

Compliance with Ethical Standards

Conflict of Interest: The authors declare that they have no conflict of interest.

References

1. Mukerjee S, Srinivasan S, Soriaga MP, McBreen J (1995) Role of structural and electronic properties of Pt and Pt alloys on electrocatalysis of oxygen reduction: An in situ XANES and EXAFS investigation. J Electrochem Soc 142:1409-1422

2. Toda T, Igarashi H, Uchida H, Watanabe M (1999) Enhancement of the electroreduction of oxygen on Pt alloys with Fe, Ni, and Co. J Electrochem Soc 146:3750-3756

3. Paulus UA, Wokaun A, Scherer GG, Schmidt TJ, Stamenkovic V, Radmilovic V, Markovic NM, Ross PN (2002) Oxygen reduction on carbon-supported Pt-Ni and Pt-Co alloy catalysts. J Phys Chem B 106:4181-4191

4. Stamenkovic VR, Fowler B, Mun BS, Wang G, Ross PN, Lucas CA, Marković NM (2007) Improved oxygen reduction activity on $Pt_3Ni(111)$ via increased surface site availability. Science 315:493-497

5. Chen C, Kang Y, Huo Z, Zhu Z, Huang W, Xin HL, Snyder JD, Li D, Herron JA, Mavrikakis M, Chi M, More KL, Li Y, Markovic NM, Somorjai GA, Yang P, Stamenkovic VR (2014) Highly crystalline multimetallic nanoframes with three-dimensional electrocatalytic surfaces. Science 343:1339-1343

6. Escudero-Escribano M, Malacrida P, Hansen MH, Vej-Hansen UG, Velázquez-Palenzuela A, Tripkovic V, Schiøtz J, Rossmeisl J, Stephens IEL, Chorkendorff I (2016) Tuning the activity of Pt alloy electrocatalysts by means of the lanthanide contraction. Science 352:73-76

7. Greeley J, Jaramillo TF, Bonde J, Chorkendorff I, Nørskov JK (2006) Computational

high-throughput screening of electrocatalytic materials for hydrogen evolution. Nature Materials 5:909-913

8. Zhang J, Vukmirovic MB, Xu Y, Mavrikakis M, Adzic RR (2005) Controlling the catalytic activity of platinum-monolayer electrocatalysts for oxygen reduction with different substrates. Angew Chem Int Ed 44:2132-2135

9. Bu L, Zhang N, Guo S, Zhang X, Li J, Yao J, Wu T, Lu G, Ma J-Y, Su D, Huang X (2016) Biaxially strained PtPb/Pt core/shell nanoplate boosts oxygen reduction catalysis. Science 354:1410-1414

10. Koh S, Strasser P (2007) Electrocatalysis on bimetallic surfaces: Modifying catalytic reactivity for oxygen reduction by voltammetric surface dealloying. J Am Chem Soc 129:12624-12625

11. Tan TL, Wang L-L, Johnson DD, Bai K (2012) A comprehensive search for stable Pt–Pd nanoalloy configurations and their use as tunable catalysts. Nano Lett 12:4875-4880

12. Hansen M, Anderko K (1958) Constitution of Binary Alloys. McGraw-Hill, New York

13. Xu X, Zhang X, Sun H, Yang Y, Dai X, Gao J, Li X, Zhang P, Wang H-H, Yu N-F, Sun S-G (2014) Synthesis of Pt–Ni alloy nanocrystals with high-index facets and enhanced electrocatalytic properties. Angew Chem Int Ed 53:12522-12527

14. Kaatz FH, Bultheel A (2018) Size, shape, and compositional effects on the order-disorder phase transitions in Au-Cu and Pt-M (M = Fe, Co, and Ni) nanocluster alloys. Nanotechnology 29:345701

15. Kim J, Lee Y, Sun S (2010) Structurally ordered FePt nanoparticles and their enhanced catalysis for oxygen reduction reaction. J Am Chem Soc 132:4996-4997

16. Chen M, Liu JP, Sun S (2004) One-step synthesis of FePt nanoparticles with tunable size. J Am Chem Soc 126:8394-8395

17. Kim J, Rong C, Liu JP, Sun S (2009) Dispersible ferromagnetic FePt nanoparticles. Adv Mater 21:906-909

18. Wang D, Xin HL, Hovden R, Wang H, Yu Y, Muller DA, DiSalvo FJ, Abruna HD (2013) Structurally ordered intermetallic platinum-cobalt core-shell nanoparticles with enhanced activity and stability as oxygen reduction electrocatalysts. Nat Mater 12:81-87

19. Zou L, Fan J, Zhou Y, Wang C, Li J, Zou Z, Yang H (2015) Conversion of PtNi alloy from disordered to ordered for enhanced activity and durability in methanol-tolerant oxygen reduction reactions. Nano Res 8:2777-2788

20. Xiong L, Manthiram A (2004) Influence of atomic ordering on the electrocatalytic activity of Pt–Co alloys in alkaline electrolyte and proton exchange membrane fuel cells. J Mater Chem 14:1454-1460

21. Koh S, Toney MF, Strasser P (2007) Activity–stability relationships of ordered and disordered alloy phases of Pt_3Co electrocatalysts for the oxygen reduction reaction (ORR). Electrochim Acta 52:2765-2774

22. Xiong L, Manthiram A (2005) Effect of atomic ordering on the catalytic activity of carbon supported PtM (M = Fe, Co, Ni, and Cu) alloys for oxygen reduction in PEMFCs. J Electrochem

Soc 152:A697-A703

23. Min M-k, Cho J, Cho K, Kim H (2000) Particle size and alloying effects of Pt-based alloy catalysts for fuel cell applications. Electrochim Acta 45:4211-4217

24. Watanabe M, Tsurumi K, Mizukami T, Nakamura T, Stonehart P (1994) Activity and stability of ordered and disordered Co-Pt alloys for phosphoric acid fuel cells. J Electrochem Soc 141:2659-2668

25. Sugawara Y, Konno M, Muto I, Hara N (2017) Formation of Pt skin layer on ordered and Disordered Pt-Co Alloys and corrosion resistance in sulfuric acid. Electrocatalysis 9:539-549

26. Gauthier Y, Baudoing-Savois R, Rosink JJWM, Sotto M (1993) LEED study of $Pt_{25}Co_{75}$(111). Surf Sci 297:193-201

27. Bertolini JC, Massardier J (1991) On the specific reactivity of platinum segregated layers on $Pt_{80}X_{20}$ (111) (X= Ni, Co, Fe) alloys. Catal Lett 9:183-188

28. Gauthier Y, Joly Y, Baudoing R, Rundgren J (1985) Surface-sandwich segregation on nondilute bimetallic alloys: $Pt_{50}Ni_{50}$ and $Pt_{78}Ni_{22}$ probed by low-energy electron diffraction. Phys Rev B 31:6216-6218

29. Gauthier Y, Baudoing R, Lundberg M, Rundgren J (1987) Surface-sandwich segregation and multilayer relaxation on $Pt_{0.5}Ni_{0.5}$(110) measured by low-energy electron diffraction: An observation of face-related segregation reversal. Phys Rev B 35:7867-7878

30. Beermann V, Kühl S, Strasser P (2018) Tuning the Catalytic Oxygen Reduction Reaction Performance of Pt-Ni Octahedral Nanoparticles by Acid Treatments and Thermal Annealing. J

Electrochem Soc 165:J3026-J3030

31. Li J, Xi Z, Pan YT, Spendelow JS, Duchesne PN, Su D, Li Q, Yu C, Yin Z, Shen B, Kim YS, Zhang P, Sun S (2018) Fe stabilization by intermetallic L10-FePt and Pt catalysis enhancement in L10-FePt/Pt nanoparticles for efficient oxygen reduction reaction in fuel cells. J Am Chem Soc 140:2926-2932

32. Wang C, Chi M, Li D, Strmcnik D, van der Vliet D, Wang G, Komanicky V, Chang K-C, Paulikas AP, Tripkovic D, Pearson J, More KL, Markovic NM, Stamenkovic VR (2011) Design and synthesis of bimetallic electrocatalyst with multilayered Pt-skin surfaces. J Am Chem Soc 133:14396-14403

33. Singh R, Sharma A, Singh P, Balasubramanian G, Johnson DD (under review) Accelerating the computational design of high-entropy alloys. Nat Comput Sci

34. Pinski FJ, Ginatempo B, Johnson DD, Staunton JB, Stocks GM, Gyorffy BL (1991) Origins of compositional order in NiPt alloys. Phys Rev Lett 66:766-769

35. Alam A, Kraczek B, Johnson DD (2010) Structural, magnetic, and defect properties of Co-Pt-type magnetic-storage alloys: Density-functional theory study of thermal processing effects. Phys Rev B 82:024435

36. Boes JR, Gumuslu G, Miller JB, Gellman AJ, Kitchin JR (2015) Estimating bulk-composition-dependent H_2 adsorption energies on Cu_xPd_{1-x} alloy (111) surfaces. ACS Catal 5:1020-1026

37. Perdew JP, Burke K, Ernzerhof M (1996) Generalized gradient approximation made simple.

Phys Rev Lett 77:3865-3868

38. Giannozzi P, Andreussi O, Brumme T, Bunau O, Buongiorno Nardelli M, Calandra M, Car R, Cavazzoni C, Ceresoli D, Cococcioni M, Colonna N, Carnimeo I, Dal Corso A, de Gironcoli S, Delugas P, DiStasio RA, Ferretti A, Floris A, Fratesi G, Fugallo G, Gebauer R, Gerstmann U, Giustino F, Gorni T, Jia J, Kawamura M, Ko HY, Kokalj A, Küçükbenli E, Lazzeri M, Marsili M, Marzari N, Mauri F, Nguyen NL, Nguyen HV, Otero-de-la-Roza A, Paulatto L, Poncé S, Rocca D, Sabatini R, Santra B, Schlipf M, Seitsonen AP, Smogunov A, Timrov I, Thonhauser T, Umari P, Vast N, Wu X, Baroni S (2017) Advanced capabilities for materials modelling with Quantum ESPRESSO. J Phys-Condens Mat 29:465901

39. Giannozzi P, Baroni S, Bonini N, Calandra M, Car R, Cavazzoni C, Ceresoli D, Chiarotti GL, Cococcioni M, Dabo I, Dal Corso A, de Gironcoli S, Fabris S, Fratesi G, Gebauer R, Gerstmann U, Gougoussis C, Kokalj A, Lazzeri M, Martin-Samos L, Marzari N, Mauri F, Mazzarello R, Paolini S, Pasquarello A, Paulatto L, Sbraccia C, Scandolo S, Sclauzero G, Seitsonen AP, Smogunov A, Umari P, Wentzcovitch RM (2009) QUANTUM ESPRESSO: A modular and open-source software project for quantum simulations of materials. J Phys-Condens Mat 21:395502

40. Hamann DR (2013) Optimized norm-conserving Vanderbilt pseudopotentials. Phys Rev B 88:085117

41. Marzari N, Vanderbilt D, De Vita A, Payne MC (1999) Thermal contraction and disordering of the Al(110) surface. Phys Rev Lett 82:3296-3299

42. Korringa J (1947) On the calculation of the energy of a Bloch wave in a metal. Physica 13:392-400

43. Kohn W, Rostoker N (1954) Solution of the schrodinger equation in periodic lattices with an application to metallic lithium. Phys Rev 94:1111-1120

44. Stocks GM, Nicholson DMC, Shelton WA, Györffy BL, Pinski FJ, Johnson DD, Staunton JB, Ginatempo B, Turchi PEA, Sluiter M (1994) Statics and Dynamics of Alloy Phase Transformations. Springer, Boston

45. Stocks GM, Shelton WA, Nicholson DM, Pinski FJ, Ginatempo B, Barbieri A, Györffy BL, Johnson DD, Staunton JB, Turchi PEA, Sluiter M (1992) Ordered Intermetallics - Physical Metallurgy and Mechanical Behaviour. Springer, Dordrecht

46. Soven P (1967) Coherent-potential model of substitutional disordered alloys. Phys Rev 156:809-813

47. Johnson DD, Nicholson DM, Pinski FJ, Gyorffy BL, Stocks GM (1986) Density-functional theory for random alloys: Total energy within the coherent-potential approximation. Phys Rev Lett 56:2088-2091

48. Alam A, Johnson DD (2012) Structural properties and relative stability of (meta)stable ordered, partially ordered, and disordered Al-Li alloy phases. Phys Rev B 85:144202

49. Andersen OK (1975) Linear methods in band theory. Phys Rev B 12:3060-3083

50. Alam A, Johnson DD (2009) Optimal site-centered electronic structure basis set from a displaced-center expansion: Improved results via a priori estimates of saddle points in the

density. Phys Rev B 80:125123

51. Nordheim L (1931) Zur Elektronentheorie der Metalle. I. Ann Phys-Berlin 401:607-640

52. Yang X, Suash D (2009) Cuckoo Search via Lévy flights. In: 2009 World Congress on Nature & Biologically Inspired Computing (NaBIC), pp 210-214

53. Monkhorst HJ, Pack JD (1976) Special points for Brillouin-zone integrations. Phys Rev B 13:5188-5192

54. Lide DR (2004) Handbook of Chemistry and Physics: A Ready-Reference of Chemical and Physical Data. 84th ed. CRC, New York

55. Dahmani CE (1985) Thesis. Louis Pasteur University, Strasbourg

56. Parra RE, Cable JW (1980) Neutron study of magnetic-moment distribution in Ni-Pt alloys. Phys Rev B 21:5494-5504

57. Kumar U, Padmalekha KG, Mukhopadhyay PK, Paudyal D, Mookerjee A (2005) Magnetic transition in NiPt alloy systems: Experiment and theory. J Magn Magn Mater 292:234-240

58. Zarkevich NA, Johnson DD (2019) Reliable thermodynamic estimators for screening caloric materials. J Alloys Compd 802:712-722

59. Haas P, Tran F, Blaha P (2009) Calculation of the lattice constant of solids with semilocal functionals. Phys Rev B 79:085104

60. Nilsson A, Pettersson LGM, Hammer B, Bligaard T, Christensen CH, Nørskov JK (2005) The electronic structure effect in heterogeneous catalysis. Catal Lett 100:111-114

61. Stamenkovic V, Mun BS, Mayrhofer KJJ, Ross PN, Markovic NM, Rossmeisl J, Greeley J,

Nørskov JK (2006) Changing the activity of electrocatalysts for oxygen reduction by tuning the surface electronic structure. Angew Chem Int Ed 45:2897-2901

62. Gumuslu G, Kondratyuk P, Boes JR, Morreale B, Miller JB, Kitchin JR, Gellman AJ (2015) Correlation of electronic structure with catalytic activity: H_2-D_2 exchange across Cu_xPd_{1-x} composition space. ACS Catal 5:3137-3147

63. Pinski FJ, Ginatempo B, Johnson DD, Staunton JB, Stocks GM, Gyorffy BL (1992) Reply to Comment on "The Origins of compositional order in NiPt". Phys Rev Lett 68:1962-1962

64. Thirumalai H, Kitchin JR (2018) Investigating the reactivity of single atom alloys using density functional theory. Top Catal 61:462-474

65. Nahm T-U, Kim J-Y, Oh SJ, Chung SM, Park JH, Allen JW, Jeong K, Kim S (1996) Photoemission study of electronic structures of disordered Ni-Pt and Cu-Pt alloys. Phys Rev B 54:7807-7815

66. Kumar U, Mukhopadhyay PK, Sanyal B, Eriksson O, Nordblad P, Paudyal D, Tarafder K, Mookerjee A (2006) Experimental and theoretical study of annealed Ni-Pt alloys. Phys Rev B 74:064401

67. Mavrikakis M, Hammer B, Nørskov JK (1998) Effect of strain on the reactivity of metal surfaces. Phys Rev Lett 81:2819-2822

68. Kitchin JR, Nørskov JK, Barteau MA, Chen JG (2004) Role of strain and ligand effects in the modification of the electronic and chemical properties of bimetallic surfaces. Phys Rev Lett 93:156801

69. Xu Y, Ruban AV, Mavrikakis M (2004) Adsorption and dissociation of O_2 on Pt-Co and Pt-Fe Alloys. J Am Chem Soc 126:4717-4725

70. Pillay D, Johannes MD (2008) Comparison of sulfur interaction with hydrogen on Pt(111), Ni(111) and $Pt_3Ni(111)$ surfaces: The effect of intermetallic bonding. Surf Sci 602:2752-2757

71. Li X, Wan W, Kattel S, Chen JG, Wang T (2016) Selective hydrogenation of biomass-derived 2(5H)-furanone over Pt-Ni and Pt-Co bimetallic catalysts: From model surfaces to supported catalysts. J Catal 344:148-156

72. Du P, Wu P, Cai C (2017) Mechanism of methanol decomposition on the $Pt_3Ni(111)$ Surface: DFT study. J Phys Chem C 121:9348-9360

73. Hammer B, Nørskov JK (1995) Electronic factors determining the reactivity of metal surfaces. Surf Sci 343:211-220

74. Kitchin JR, Khan NA, Barteau MA, Chen JG, Yakshinskiy B, Madey TE (2003) Elucidation of the active surface and origin of the weak metal–hydrogen bond on Ni/Pt(111) bimetallic surfaces: a surface science and density functional theory study. Surf Sci 544:295-308

75. Bai Y, Kirvassilis D, Xu L, Mavrikakis M (2019) Atomic and molecular adsorption on Ni(111). Surf Sci 679:240-253

76. Greeley J, Mavrikakis M (2003) A first-principles study of surface and subsurface H on and in Ni(111): diffusional properties and coverage-dependent behavior. Surf Sci 540:215-229

77. Taylor CD, Neurock M, Scully JR (2011) A first-principles model for hydrogen uptake promoted by sulfur on Ni(111). J Electrochem Soc 158:F36

78. Wellendorff J, Silbaugh TL, Garcia-Pintos D, Nørskov JK, Bligaard T, Studt F, Campbell CT (2015) A benchmark database for adsorption bond energies to transition metal surfaces and comparison to selected DFT functionals. Surf Sci 640:36-44

79. Hoster HE, Janik MJ, Neurock M, Behm RJ (2010) Pt promotion and spill-over processes during deposition and desorption of upd-H_{ad} and OH_{ad} on Pt_xRu_{1-x}/Ru(0001) surface alloys. Phys Chem Chem Phys 12:10388-10397

80. Ford DC, Xu Y, Mavrikakis M (2005) Atomic and molecular adsorption on Pt(111). Surf Sci 587:159-174

81. Su HY, Bao XH, Li WX (2008) Modulating the reactivity of Ni-containing Pt(111)-skin catalysts by density functional theory calculations. J Chem Phys 128:194707

82. Papoian G, Nørskov JK, Hoffmann R (2000) A comparative theoretical study of the hydrogen, methyl, and ethyl chemisorption on the Pt(111) surface. J Am Chem Soc 122:4129-4144

83. Wang G-C, Zhou Y-H, Morikawa Y, Nakamura J, Cai Z-S, Zhao X-Z (2005) Kinetic mechanism of methanol decomposition on Ni(111) surface: A theoretical study. J Phys Chem B 109:12431-12442

84. Shin YK, Gai L, Raman S, van Duin ACT (2016) Development of a ReaxFF reactive force field for the Pt-Ni alloy catalyst. J Phys Chem A 120:8044-8055

85. Hamada I, Morikawa Y (2008) Density-functional analysis of hydrogen on Pt(111): Electric field, solvent, and coverage effects. J Phys Chem C 112:10889-10898

86. Lapujoulade J, Neil KS (1972) Chemisorption of hydrogen on the (111) plane of nickel. J Chem Phys 57:3535-3545

87. Christmann K, Schober O, Ertl G, Neumann M (1974) Adsorption of hydrogen on nickel single crystal surfaces. J Chem Phys 60:4528-4540

88. Poelsema B, Mechtersheimer G, Comsa G (1981) The interaction of hydrogen with platinum(s)−9(111)×(111) studied with helium beam diffraction. Surf Sci 111:519-544

89. Hoffmannová H, Okube M, Petrykin V, Krtil P, Mueller JE, Jacob T (2013) Surface stability of Pt_3Ni nanoparticulate alloy electrocatalysts in hydrogen adsorption. Langmuir 29:9046-9050

90. Zhang L, Anderson RM, Crooks RM, Henkelman G (2015) Correlating structure and function of metal nanoparticles for catalysis. Surf Sci 640:65-72

91. Zhang L, Henkelman G (2015) Computational design of alloy-core@shell metal nanoparticle catalysts. ACS Catal 5:655-660

92. Friebel D, Viswanathan V, Miller DJ, Anniyev T, Ogasawara H, Larsen AH, O'Grady CP, Nørskov JK, Nilsson A (2012) Balance of nanostructure and bimetallic interactions in Pt model fuel cell catalysts: In situ XAS and DFT study. J Am Chem Soc 134:9664-9671

93. Xin H, Linic S (2010) Communications: Exceptions to the d-band model of chemisorption on metal surfaces: The dominant role of repulsion between adsorbate states and metal d-states. J Chem Phys 132:221101

94. Xin H, Schweitzer N, Nikolla E, Linic S (2010) Communications: Developing relationships between the local chemical reactivity of alloy catalysts and physical characteristics of constituent

metal elements. J Chem Phys 132:111101

95. Wang LL, Johnson DD (2008) Electrocatalytic properties of PtBi and PtPb intermetallic line compounds via DFT: CO and H adsorption. J Phys Chem C 112:8266-8275

96. Hartmann H, Diemant T, Bergbreiter A, Bansmann J, Hoster HE, Behm RJ (2009) Surface alloy formation, short-range order, and deuterium adsorption properties of monolayer PdRu/Ru(0001) surface alloys. Surf Sci 603:1439-1455